A semi-analytical model to estimate Chlorophyll-a spatial-temporal patterns from Orbita Hyperspectral image in inland eutrophic waters

Science of the Total Environment

Zheng, Zhubin; Huang, Chao; Li, Yunmei; Lyu, Heng; Huang, Changchun et al

https://doi.org/10.1016/j.scitotenv.2023.166785

This publication is made publicly available in the institutional repository of Wageningen University and Research, under the terms of article 25fa of the Dutch Copyright Act, also known as the Amendment Taverne.

Article 25fa states that the author of a short scientific work funded either wholly or partially by Dutch public funds is entitled to make that work publicly available for no consideration following a reasonable period of time after the work was first published, provided that clear reference is made to the source of the first publication of the work.

This publication is distributed using the principles as determined in the Association of Universities in the Netherlands (VSNU) 'Article 25fa implementation' project. According to these principles research outputs of researchers employed by Dutch Universities that comply with the legal requirements of Article 25fa of the Dutch Copyright Act are distributed online and free of cost or other barriers in institutional repositories. Research outputs are distributed six months after their first online publication in the original published version and with proper attribution to the source of the original publication.

You are permitted to download and use the publication for personal purposes. All rights remain with the author(s) and / or copyright owner(s) of this work. Any use of the publication or parts of it other than authorised under article 25fa of the Dutch Copyright act is prohibited. Wageningen University & Research and the author(s) of this publication shall not be held responsible or liable for any damages resulting from your (re)use of this publication.

For questions regarding the public availability of this publication please contact
openaccess.library@wur.nl

Science of the Total Environment 904 (2023) 166785

Contents lists available at ScienceDirect

Science of the Total Environment

journal homepage: www.elsevier.com/locate/scitotenv

A semi-analytical model to estimate Chlorophyll-a spatial-temporal patterns from Orbita Hyperspectral image in inland eutrophic waters

Zhubin Zheng [a,*,1], Chao Huang [a,1], Yunmei Li [b], Heng Lyu [b], Changchun Huang [b], Na Chen [c], Ge Liu [d], Yulong Guo [e], Shaohua Lei [f], Runfei Zhang [b], Jianzhong Li [b]

[a] *School of Geography and Environmental Engineering, Jiangxi Provincial Key Laboratory of Low-Carbon Solid Waste Recycling, Gannan Normal University, Ganzhou 341000, China*
[b] *School of Geographic Science, Key Laboratory of Virtual Geographic Environment of Education Ministry, Nanjing Normal University, Nanjing 210023, China*
[c] *Department of Environmental Sciences, Laboratory of Geo-Information Science and Remote Sensing, Wageningen University & Research, Droevendaalsesteeg 3, 6708 PB Wageningen, the Netherlands*
[d] *Northeast Institute of Geography and Agroecology, Chinese Academy of Sciences, Changchun 130102, China*
[e] *College of the Resources and Environmental Sciences, Henan Agricultural University, Zhengzhou 450002, China*
[f] *State Key Laboratory of Hydrology-Water Resources and Hydraulic Engineering, Nanjing Hydraulic Research Institute, Nanjing 210029, China*

HIGHLIGHTS

- A novel quasi-analytical algorithm (QAA_{716}) produced robust results.
- OHS images documented significant spatial-temporal patterns of Chl-a.
- Total nitrogen was the key factor affecting the Chl-a variations in Dianchi Lake.
- The OHS images' improved signal-to-noise ratio expedited the retrieval of Chl-a.

GRAPHICAL ABSTRACT

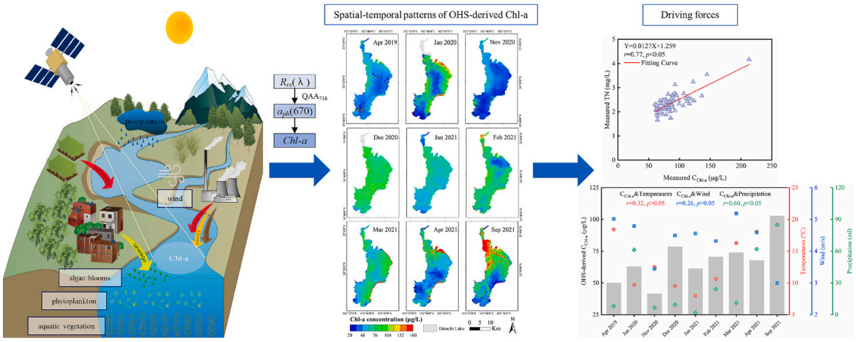

ARTICLE INFO

Editor: Ashantha Goonetilleke

Keywords:
Semi-analytical mode
Orbita Hyperspectral image
Chlorophyll-a
Spatial-temporal patterns
Noise-equivalent Chlorophyll-a

ABSTRACT

It can be challenging to accurately estimate the Chlorophyll-a (Chl-a) concentration in inland eutrophic lakes due to lakes' extremely complex optical properties. The Orbita Hyperspectral (OHS) satellite, with its high spatial resolution (10 m), high spectral resolution (2.5 nm), and high temporal resolution (2.5 d), has great potential for estimating the Chl-a concentration in inland eutrophic waters. However, the estimation capability and radiometric performance of OHS have received limited examination. In this study, we developed a new quasi-analytical algorithm (QAA_{716}) for estimating Chl-a using OHS images. Based on the optical properties in Dianchi Lake, the ability of OHS to remotely estimate Chl-a was evaluated by comparing the signal-to-noise ratio (SNR) and the noise equivalent of Chl-a ($NE_{Chl\text{-}a}$). The main findings are as follows: (1) QAA_{716} achieved significantly better results than those of the other three QAA models, and the Chl-a estimation model, using QAA_{716}, produced robust results with a mean absolute percentage difference (MAPD) of 11.54 %, which was

---

* Corresponding author.
E-mail address: zhengzhubin@gnnu.edu.cn (Z. Zheng).
[1] These authors contributed equally to this study.

https://doi.org/10.1016/j.scitotenv.2023.166785
Received 29 May 2023; Received in revised form 1 September 2023; Accepted 1 September 2023
Available online 4 September 2023

better than existing Chl-a estimation models; (2) The FLAASH (Fast Line-of-sight Atmospheric Analysis of Spectral Hypercubes) atmospheric correction model (MAPD = 22.22 %) was more suitable for OHS image compared to the other three atmospheric correction models we tested; (3) OHS had relatively moderate SNR and $NE_{Chl\text{-}a}$, improving its ability to accurately detect Chl-a concentration and resulting in an average SNR of 59.47 and average $NE_{Chl\text{-}a}$ of 72.86 μg/L; (4) The increased Chl-a concentration in Dianchi Lake was primarily related to the nutrients input, and this had a significant positive correlation with total nitrogen. These findings expand existing knowledge of the capabilities and limitations of OHS in remotely estimating Chl-a, thereby facilitating effective water quality management in eutrophic lake environments.

1. Introduction

Chlorophyll-a (Chl-a) is an important optically active constituent (OAC) that directly correlates with the primary productivity of phytoplankton. This makes it an essential indicator for assessing water quality and nutrient status (Beck et al., 2016; Ekstrand, 1992; Yang et al., 2010). Chl-a concentration ($C_{Chl\text{-}a}$) can be accurately measured in the field, but doing so is time-consuming and laborious, creating difficulty when monitoring large lakes over extended periods of time. Satellite remote sensing provides a promising solution for long-term and wide-spread monitoring of $C_{Chl\text{-}a}$ in various environments (Lee et al., 2016; Li et al., 2019; Mishra et al., 2013; Yao et al., 2020).

Numerous remote sensing algorithms have been developed to quantify $C_{Chl\text{-}a}$ in inland waters, most being empirical. Additionally, machine learning has been used to retrieve $C_{Chl\text{-}a}$ levels (Cao et al., 2020; Cao et al., 2022a). However, these methods usually lack a theoretical basis and are often used for multispectral images, especially with the development of hyperspectral images. Several algorithms based on hyperspectral data have been proposed, such as the Chl-a three-band model (Hu et al., 2012b; O'Reilly et al., 1998) and the four-band model (Le et al., 2013), developed for turbid waters. The spectral features of $C_{Chl\text{-}a}$ have also been used in $C_{Chl\text{-}a}$ retrieval (Bi et al., 2018a; Liu and Tang, 2019; Lyu et al., 2015). However, the above algorithms often rely on assumptions and lack a mechanistic investigation of Chl-a. The a_{ph} (absorption coefficient of phytoplankton) is closely related to $C_{Chl\text{-}a}$ through its specific absorption characteristics (Bricaud et al., 1995; Nardelli and Twardowski, 2016) and can be used as a proxy parameter in the estimation of $C_{Chl\text{-}a}$ (Jiang et al., 2021; Liu et al., 2020). Liu et al. (2020) developed an improved quasi-analytical algorithm (TC2) that uses a_{ph} to estimate the $C_{Chl\text{-}a}$ for Case-II turbid waters. However, TC2 requires extensive measurement data and produces unsatisfactory results in eutrophic waters. Despite this limitation, TC2 enabled a direct investigation into the mechanistic changes of $C_{Chl\text{-}a}$ using a_{ph}, indicating comprehensive explanation and generalizability. The quasi-analytical algorithm (QAA), developed by Lee et al. (2002), has been widely used to derive the inherent optical properties (IOPs) of oceanic waters (Liu et al., 2020; Shi et al., 2019). Even so, it has shown limitations in Case-II waters, rerating the reference band, and re-parametrizing the equation to produce more reasonable results in turbid waters (Rodrigues et al., 2017; Wang et al., 2009).

Inland waters have relatively complex optical properties, and unstable factors such as climatic change and anthropogenic activities can affect $C_{Chl\text{-}a}$ in eutrophic waters, making it challenging for multispectral remote sensing to accurately capture their spectral characteristics (Zheng et al., 2022). Hyperspectral satellites, such as PRISMA (PRecursore IperSpettrale della Missione Applicativa), OLCI (Ocean and Land Color Instrument), DESIS (DLR Earth Sensing Imaging Spectrometer), and HICO (Hyperspectral Imager for the Coastal Ocean), have shown promising performances in water quality monitoring within various environments (Bresciani et al., 2022; Lima et al., 2023; O'Shea et al., 2021). The Orbita Hyperspectral (OHS) satellite, launched in China, has in-orbit image (Complementary Metal-Oxide-Semiconductor, CMOS) technology that combines high spectral resolution (2.5 nm), high spatial resolution (10 m), and high temporal resolution (2.5 d), with 256 spectral bands (32 optional band width at 5–14 nm) within a band range of 400–1000 nm. This makes it suitable for detecting water quality in inland eutrophic lakes (Cao et al., 2019; Zhong et al., 2021). The three high resolutions of OHS make it highly sensitive to the optical characteristics of complex and dynamically variable inland waters, thereby enhancing its ability to monitor inland water quality (Kutser et al., 2001). However, the assessment of OHS's capability to monitor water quality parameters is limited (Zhang et al., 2021).

The main objective of this study is to evaluate the $C_{Chl\text{-}a}$ spatial-temporal patterns in eutrophic lake using OHS images and the semi-analytical model. Specifically, our aims are: (1) To develop a re-parametrized QAA model (QAA_{716}) that could estimate $C_{Chl\text{-}a}$, based on the characteristics of eutrophic waters; (2) to evaluate the feasibility and radiometric capability of $C_{Chl\text{-}a}$ measurements using OHS images; (3) to explore the spatial-temporal patterns of $C_{Chl\text{-}a}$ in Dianchi Lake.

2. Materials and methods

2.1. Study area

Dianchi Lake (Fig. 1), the largest freshwater lake (330 km^2) in the Yunnan-Guizhou Plateau region, is located southwest of Kunming City, Yunnan Province. It plays a crucial role for both residents and the environment. Unfortunately, Dianchi Lake's water environment and aquatic ecosystem have suffered serious damage in recent years due to rapid economic development, urbanization, and population pressure. This has resulted in a continuous decline in water quality and an increase in nutrient levels (Yang et al., 2018), making it one of the most environmentally polluted lakes in China (Liu et al., 2015; Yang et al., 2018). Despite attempts to clean up the lake, Dianchi Lake remains at an extremely eutrophic level, emphasizing the importance of monitoring its water quality.

2.2. Data and processing

2.2.1. Field data

Two field campaigns were conducted on April 13–16, 2017 and November 13–15, 2017. A total of seventy-one remote sensing reflectance (R_{rs}), Secchi-disk depth (SD), and water samples were selected and studied (Fig. 1c). R_{rs} spectra were measured with ASD FieldSpec Pro portable spectrometer (ASD Inc., Boulder, CO, USA). The observation geometry with an azimuth of the Sun of 135° and a nadir angle of 40° (Mobley, 1999; Mueller et al., 2003). The SD was measured at the sample sites using a standard Secchi-disk with a diameter of 30 cm (Preisendorfer, 1986). Water samples from each site (0.5 m depth) were collected for laboratory analysis, and the longitude and latitude were recorded using global positioning system receivers. Additionally, the Dianchi Lake Administration provided measured $C_{Chl\text{-}a}$ for April 2, 2019 (N = 9), and China National Environmental Monitoring Centre provided measured $C_{Chl\text{-}a}$ data for March 19 (N = 5), March 26 (N = 4), and April 16 (N = 7), 2021. A total of 25 in-situ $C_{Chl\text{-}a}$ measurements were synchronized with the OHS observation. R_{rs} was derived through the following equation (Tang et al., 2004):

$$R_{rs}(\lambda) = \frac{\left(L_w - \rho L_{sky}\right)^* R_g}{L_g \pi} \tag{1}$$

where L_w, L_{sky}, L_g, and R_g denote the total radiance measured on the water surface, the radiance of the skylight, the radiance of the reference panel, and the reflectance of the gray diffuse panel (30 %), respectively; ρ represents the skylight reflectance at the air-water interface and the impact of wind (2.2 % for calm water surface, 2.5 % for 5 m/s, 2.6 %–2.8 % for 10 m/s).

A total of seventy-one water samples were taken to the laboratory to measure water quality parameters (Chl-a, total suspended matter (TSM), total phosphorus (TP), and total nitrogen (TN)) and optical parameters (absorption coefficient of particulates (a_p), absorption coefficient of phytoplankton (a_{ph}), absorption coefficient of non-algal particulates (a_{NAP}), and absorption coefficient of chromophoric dissolved organic matter (a_{CDOM})). After the water samples' phytoplankton pigments were extracted using 90 % hot ethanol at 80 °C and acidified with 1 % diluted hydrochloric acid, the concentrations of Chl-a were measured using spectrophotometric techniques (Jespersen and Christoffersen, 1987). Water samples were filtered through fiberglass filters (Whatman GF/F, 0.7 μm pore-size) and pre-combusted at 550 °C for 4 h to remove organic traces and dried at 105 °C for 4 h and then weighed to obtain the concentrations of TSM using the gravimetric method (Zheng et al., 2016). The concentrations of TP and TN were measured using a UV-VIS spectrophotometer (Etheridge et al., 2014; Huang et al., 2015). Absorption coefficient components were measured using the quantitative filtering technique (QFT) (Brian Gregory, 1990; Prieur and Sathyendranath, 1981).

2.2.2. Climatic data

The monthly averages of temperature, precipitation, and wind speed data were collected from the Kunming meteorological station in Kunming City (Fig. 1c). These data were downloaded from the National Oceanic and Atmospheric Administration from 2019 to 2021 (https://www1.ncdc.noaa.gov/pub/data/paleo/).

2.2.3. Satellite data and processing

In this study, OHS Level-1A (Digital Number) data, including radiometric calibration data for the sensor, were obtained from Zhuhai Orbita Aerospace Technology Co., Ltd. From April 2, 2019 to September 13, 2021, with a total of 10 cloudless OHS images collected over Dianchi Lake (https://ohs.obtdata.com/). To calculate the radiometric performance of OHS imagery, Fuxian Lake, a clean body of water, was used for the signal-to-noise ratio (SNR) estimation (Fig. 1d) (Cao et al., 2022b). The Landsat-9 OLI2 (Operational Land Imager 2), a new generation satellite in the Landsat family, was used for the $C_{Chl\text{-}a}$ retrieval by Cao et al. (2022b), but its radiation performance lacked sufficient research. The OLI-2 imagery of an open and cloudless ocean area was collected on April 9, 2023 (https://glovis.usgs.gov/), and the details of the SNR area were estimated (Cao et al., 2018). Additionally, Hyperion imagery collected on October 22, 2009, as OLI2 describes, was used to compare the radiometric performance with another hyperspectral image (https://glovis.usgs.gov/).

To determine the suitable atmospheric correction (AC) model for OHS imagery, four different AC models were used: the FLAASH (Fast Line-of-sight Atmospheric Analysis of Spectral Hypercubes) model, the QUAC (Quick Atmospheric Correction) model, the 6S (Second Simulation of Satellite Signal in the Solar Spectrum) model, and the DOS (Dark Object Subtraction) model. The details of the AC models are found in Zhang et al. (2021). The FLAASH Guide Setting in ENVI (Environment for Visualizing Images) 5.3 was used to determine parameters, such as the aerosol models. The QUAC and DOS models were integrated into ENVI 5.3 and automatically selected parameters. The 6S model was applied in the OPENOHS, a software specifically designed for processing OHS imagery (https://www.obtdata.com/#/content/scheme/userGuide). The user only needs to select the aerosol model. The continental aerosol model was also used for the 6S model (Bi et al., 2018b). After atmospheric correction, a geometric deviation of OHS (<1 km) was discovered. As a result, all OHS images underwent calibration, using

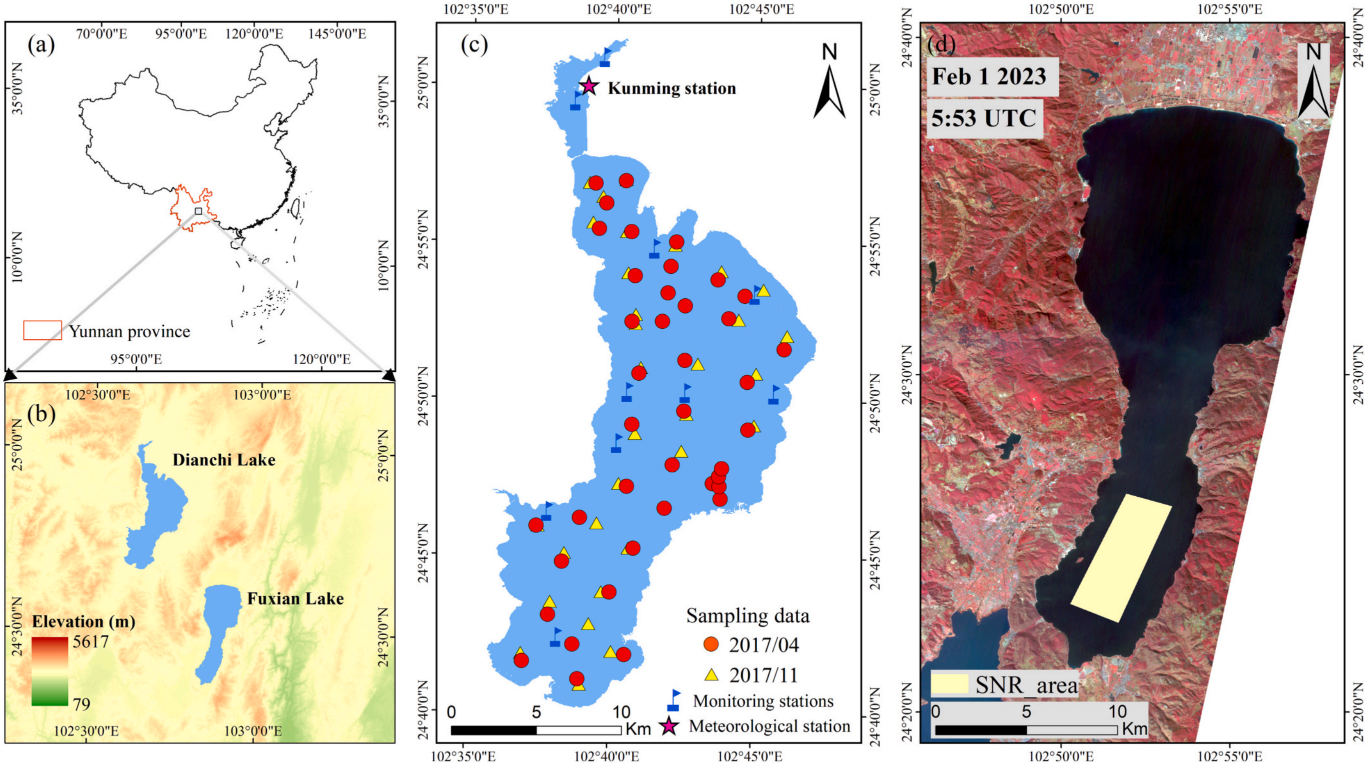

Fig. 1. Location and sampling data distribution of Dianchi Lake in China. (a) Location of study area in China; (b) distribution of Dianchi Lake and Fuxian Lake; (c) distribution of sampling data in Dianchi Lake; (d) distribution of signal-to-noise ratio (SNR) calculation area (yellow symbol) in the Fuxian Lake obtained by Orbita Hyperspectral image on February 1, 2023.

the orthorectification tool in the OPENOHS. To assess the effectiveness of AC model for OHS images, satellite-ground synchronous measured $C_{Chl\text{-}a}$ were used to compare with OHS-derived $C_{Chl\text{-}a}$ obtained by different AC models.

2.3. Semi-analytical model development

2.3.1. Relationship between Chl-a and $a_{ph}(\lambda)$

For the Chl-a retrieval, $C_{Chl\text{-}a}$ can be expressed as (Liu et al., 2020):

$$C_{Chl-a} = \frac{a_{ph}(\lambda)}{a_{ph}^{*}(\lambda)} \tag{2}$$

where $a_{ph}^{*}(\lambda)$ is the absorption per unit $C_{Chl\text{-}a}$. Previous researches (Bricaud et al., 1995; Ciotti et al., 2002) had shown that the values of $a_{ph}^{*}(\lambda)$ are connected to cell size, intracellular pigment concentration variations, and photoadaptation within the local population. Accurately calculating these values was difficult and required a massive number of estimates on a regional or global scale. However, there is a strong correlation between $C_{Chl\text{-}a}$ and $a_{ph}(\lambda)$, allowing for the development of an empirical relationship that estimated $a_{ph}(\lambda)$ as a function of $C_{Chl\text{-}a}$. Thus, Eq. (2) can be rewritten as (Cleveland, 1995):

$$C_{Chl-a} \propto a_{ph}(\lambda) \tag{3}$$

where the wavelength λ was usually the $a_{ph}(\lambda)$ peak at the red band for inland waters (Liu et al., 2020). For our purposes, the relationship between $a_{ph}(\lambda)$ and $C_{Chl\text{-}a}$ was firstly analyzed, and the wavelength with the highest correlation was chosen. After making the necessary modifications, $C_{Chl\text{-}a}$ could be obtained from the $a_{ph}(\lambda)$. After deriving $a_{ph}(\lambda)$ from the R_{rs} using QAA, a total of 71 $C_{Chl\text{-}a}$ data were randomly divided into modeling data sets (N = 48) and validation data sets (N = 23) to construct and validate the Chl-a estimation model (Fig. 3).

2.3.2. Improving QAA model for deriving $a_{ph}(\lambda)$

Lee et al. (2002) developed the QAA model to establish the relationship between R_{rs} and IOPs based on theoretical analysis and numerical simulation of the radiative transfer models (Lee et al., 2002; Lee et al., 2014a). The QAA consists of two primary parts: the inversion step, which yields the a (total absorption coefficient) and b_{bp} (backscattering coefficient of particulates) at each wavelength, and the partition step, which yields the a_{ph} and a_{dg} (absorption coefficient of colored dissolved organic matter and detritus). The QAA model has been updated to its sixth version (QAA_{670}). However, researchers have found that directly applying QAA_{670} estimate a and b_{bp} for lakes following ocean waters assumption may lead to significant underestimation, due to the distinct optical characteristics among different bodies of water (Rodrigues et al., 2017; Zhang et al., 2012).

Therefore, the main goals in developing the QAA_{716} model for Dianchi Lake were: (1) Adjusting the original reference band to ensure that the original assumption (absorption coefficient of pure water, a_w, dominates absorption at the reference band) remained applicable at the adjusted reference band; (2) incorporating the measured IOPs specific to Dianchi Lake for re-parameterization (Huang et al., 2014; Ogashawara et al., 2016; Rodrigues et al., 2017; Watanabe et al., 2016; Yang et al., 2013); (3) referring the band settings and central wavelengths for OHS images. The improved steps of the QAA_{716} are as follows (Zheng, 2018):

Improved step 1: Based on the measured optical characteristics in Dianchi Lake and the theoretical foundation of the reference wavelength proposed by Lee et al. (2002), the reference wavelength in this study was redefined as 716 nm. The reasons were as follows: (a) In QAA_{670}, the reference wavelength was 670 nm, where the a_p dominated the absorption in Dianchi Lake; (b) at 716 nm, the a_w dominated the absorption in Dianchi Lake; (c) the a_{CDOM} at 716 nm was negligible compared to a_w; (d) the central wavelength of the near-infrared band of the OHS was at 716 nm. Consequently, the $a(716)$ can be calculated as:

$$\begin{aligned} a(\lambda_0) &= a_w(\lambda_0) + \Delta a(\lambda) \\ &= a_w(716) + \alpha\frac{r_{rs}(555)}{r_{rs}(710)} + \beta\frac{r_{rs}(670)}{r_{rs}(710)} + \gamma\frac{r_{rs}(760)}{r_{rs}(555)} \\ \alpha &= -0.649, \beta = 1.149, \gamma = 0.037 \end{aligned} \tag{4}$$

where $r_{rs}(\lambda)$ is the lower-water surface remote sensing reflectance and $\Delta a(\lambda)$ is the sum of the absorption of OAC. The b_{bw} (backscattering coefficient of pure water) was negligible compared to the b_{bp} in Dianchi Lake, while the a at 716 nm can be roughly estimated from a_w in this band. The coefficient in the $\Delta a(\lambda)$ function was determined by referring to the method proposed by Mishra et al. (2013) and Rodrigues et al. (2017).

Improved step 2: After reselecting the new reference band, $b_{bp}(716)$ can be obtained as follows:

$$b_{bp}(716) = \frac{u(716) \times a(716)}{1 - u(716)} - b_{bw}(716) \tag{5}$$

Improved step 3: Calculating the probability of the η (particle backscattering coefficient), an empirical value calculated from in-situ measurement data. For oceanic Case-I waters, Lee et al. (2002) considered η values as 0–1, and 1–2 for Case-II waters. For Dianchi Lake, there were no established numbers to determine the range of η values. Therefore, this study referred to Lee et al. (1998) and used a band optimization algorithm. Initially, 760 nm was used as the denominator, and the numerator varied from 400 to 800 nm. Eventually, 555 nm was determined to be the optimal band. As a result, η can be calculated from the following equation:

$$\eta = 2.0 \times \left[1 - 1.2 \times e^{\left(-0.9 \times \frac{r_{rs}(555)}{r_{rs}(760)}\right)}\right] \tag{6}$$

Based on the aforementioned steps, the values of a, a_{ph}, and b_{bp} at any wavelength can be derived by calculating the values of a and b_{bp} at the reference wavelength (Table 1). The reference band used in this study, 716 nm, was similar to that seen with turbid waters in previous studies, such as Taihu Lake and Poyang Lake (Huang et al., 2014; Le et al., 2009). This indicated that the original assumptions of the QAA_{670} were not applicable in lakes like Dianchi Lake. Thus, the reference band needed to be rerated and then re-parametrized.

2.3.3. Generating virtual bands from OHS image

Despite having 32 bands, the OHS image lacked two bands centered at 412 nm and 443 nm, which were crucial for deriving a_{ph} with the QAA model. Fortunately, Wei et al. (2019) proposed an algorithm for estimating the reflectance of the virtual band. The virtual band at 443 nm can be obtained using Wei et al.'s example of estimating the virtual band at 412 nm. This is illustrated in the succeeding paragraphs.

First, the in-situ R_{rs} and the spectral response function (SRF) were convolved spectrally to obtain $R_{rs}(B_i)$:

$$R_{rs}(B_i) = \frac{\int_{400}^{800} SRF(\lambda) R_{rs}(\lambda) d\lambda}{\int_{400}^{800} SRF(\lambda) d\lambda}, i = 1, 2, \cdots, 32 \tag{7}$$

where SRF represents the OHS's spectral response function for each band. $R_{rs}(B_0)$ was derived by assuming a bandwidth of 5 nm for the virtual band and interpolating hyperspectral data at 412 nm.

Next, the 33 bands of each sample point were normalized by the arithmetic square root of B_0 to B_{32} (Wei et al., 2016):

Table 1

QAA$_{716}$ remote sensing estimation steps. Steps with a gray background indicate improvements proposed in this study. $u(\lambda)$ is a function of the a and b_b. ξ, S, and ζ are all parameters from Lee et al. (2014a).

Part	Step	Equations	Method
Part I	1	$r_{rs}(\lambda)=R_{rs}(\lambda)/(0.52+1.7\times R_{rs}(\lambda))$	Semi-analytical
	2	$u(\lambda)=\frac{-g_0+\sqrt{{g_0}^2+4g_1\times r_{rs}(\lambda)}}{2g_1}$ $g_0=0.089, g_1=0.125$	Semi-analytical
	3	$a(\lambda_0)=a_w(\lambda_0)+\Delta a(\lambda)$ $=a_w(716)+\alpha\frac{r_{rs}(555)}{r_{rs}(710)}+\beta\frac{r_{rs}(670)}{r_{rs}(710)}+\gamma\frac{r_{rs}(760)}{r_{rs}(555)}$ $\alpha=-0.649, \beta=1.149, \gamma=0.037$	Empirical
	4	$b_{bp}(716)=\frac{u(716)\times a(716)}{1-u(716)}-b_{bw}(716)$	Analytical
	5	$\eta=2.0\times[1-1.2\times e^{(-0.9\times\frac{r_{rs}(555)}{r_{rs}(760)})}]$	Empirical
	6	$b_{bp}(\lambda)=b_{bp}(\lambda_0)\times\left[\frac{\lambda_0}{\lambda}\right]^{\eta}$	Semi-analytical
	7	$a(\lambda)=\frac{[1-u(\lambda)]\times[b_{bw}(\lambda)+b_{bp}(\lambda)]}{u(\lambda)}$	Analytical
Part II	8	$\zeta=0.74+\frac{0.2}{0.8+r_{rs}(443)/r_{rs}(555)}$ $S=0.015+\frac{0.002}{0.6+r_{rs}(443)/r_{rs}(555)}$ $\xi=e^{S(442.5-415.5)}$	Semi-analytical
	9	$a_{dg}(443)=\frac{a(412)-\zeta\times a(443)}{\xi-\zeta}-\frac{a_w(412)-\zeta\times a_w(443)}{\xi-\zeta}$ $a_{dg}(\lambda)=a_{dg}(443)e^{-S(\lambda-443)}$ $a_{ph}(\lambda)=a(\lambda)-a_{dg}(\lambda)-a_w(\lambda)$	Semi-analytical

$$nR^{*}_{rs}(B_i)=\frac{R_{rs}(B_i)}{\left[\sum_{j=0}^{32}R_{rs}(B_j)^2\right]^{\frac{1}{2}}}, i=0,1,2,\cdots,32 \tag{8}$$

where $nR^{*}_{rs}(B_i)$ is the normalized R_{rs}. The $nR^{*}_{rs}(B_i)$ spectra were used to represent the shape of the spectra in the OHS-detected inland waters.

By resolving the distances of $R_{rs}(B_0)$ and $nR^{*}_{rs}(B_i)$, $R_{rs}(B_0)$ can be determined as:

$$R_{rs}(B_0)=D\times nR^{*}_{rs}(412) \tag{9}$$

where D is the scaling factor (Wei et al., 2019):

$$D=\left[\sum_{i=1}^{32}R_{rs}(B_i)^2\right]^{\frac{1}{2}}\Big/\left[\sum_{k=1}^{32}R^{*}_{rs}(B_k)^2\right]^{\frac{1}{2}} \tag{10}$$

Based on the estimated $R_{rs}(412)$ and $R_{rs}(443)$ bands, the OHS was able to derive the source of the separation of a_{ph}. Both R^2 values for $R_{rs}(412)$ and $R_{rs}(443)$ are 0.95, and the values fall within the 95 % prediction band. This indicates that $R_{rs}(412)$ and $R_{rs}(443)$ could be derived from $R_{rs}(466)$ using a relationship, making it feasible to use QAA$_{716}$ to yield a_{ph} from OHS data (Yin et al., 2021). The results and data are depicted in Fig. S1.

2.4. Image evaluation

The SNR is a crucial sensor evaluation parameter, in which a higher SNR denotes less noise, less uncertainty, and greater accuracy (Cao et al., 2018). The local variance method was used to determine the SNR of the OHS images (Cao et al., 2018). Fuxian Lake, a clean water body in the Yunnan-Guizhou Plateau region (Fig. 1b), was selected for the SNR estimation (Cao et al., 2022b). The main steps were: (1) Using the Canny operator to extract the pure window of the image (Fig. 1d); (2) Screening the image pixels in the range within a 3*3 window, with a threshold set at 1.002 (Hu et al., 2012a); (3) Calculating the standard deviation within this region as the 'noise estimate' (*LSD*) and determining the mean value as the 'signal estimate' (*DN*). The SNR was calculated as follows:

$$SNR=\frac{DN}{LSD} \tag{11}$$

The remote estimation of C$_{\text{Chl-a}}$ relied on both algorithm accuracy and the quality of remote sensing images. Previous studies have evaluated noise-equivalent studies using empirical bands (Ren et al., 2018; Vanhellemont and Ruddick, 2014). Consequently, a new noise-equivalent Chl-a ($NE_{Chl\text{-}a}$) was proposed to evaluate the ability of the imagery based on the semi-analytical model.

To quantitatively assess and compare the radiometric performance of different images and the uncertainty caused by noise, the noise equivalent reflectance (NE_{ρ}) was calculated as follows (Vanhellemont and Ruddick, 2014):

$$NE_{\rho}=\frac{\pi\times NE_L\times d^2}{F_0\times cos\theta} \tag{12}$$

where NE_L is the noise equivalent irradiance (Eq. (13)), d is the Sun-to-Earth astronomical distance, approximated by 1 AU (Astronomical Unit), F_0 is the extraterrestrial solar irradiance, and θ is the solar zenith angle. The NE_L was calculated as follows:

$$NE_L=\frac{L_{ref}}{SNR} \tag{13}$$

where L_{ref} is the radiance of the reference wavelength, and SNR is the SNR at the L_{ref}. The $NE_{Chl\text{-}a}$ was calculated using the Chl-a semi-analytical model proposed in this study.

2.5. Accuracy evaluation

Several indicators were used for statistical analysis: (1) The Pearson correlation coefficient (r), and the coefficient of determination (R^2) were used to determine the relationship between two variables; (2) p-value was used to detect significance ($p < 0.05$) or non-significance ($p > 0.05$); (3) the mean absolute percentage difference (MAPD) and the root mean square difference (RMSD) were used to demonstrate the statistical accuracy of the model. The equations are as follows (Li et al., 2023; Zheng et al., 2016):

$$MAPD=\frac{1}{N}\sum_{i,j=1}^{N}\left|\frac{X_i-X_j}{X_i}\right|\times 100\% \tag{14}$$

$$RMSD=\sqrt{\frac{1}{N}\sum_{i,j=1}^{N}(X_i-X_j)^2} \tag{15}$$

where N is the number of samples, and X_i and X_j are the derived and measured values, respectively. The r, R^2, and p-values were used in the C$_{\text{Chl-a}}$ model's calibration and driving force analysis (Figs. 3, S3, S4, S5, Table S1). MAPD and RMSD were used in model validation. Fig. 2 shows the validation of QAA$_{716}$, while Figs. 3, 4, S5, S6, and Table S1 show C$_{\text{Chl-a}}$'s validation.

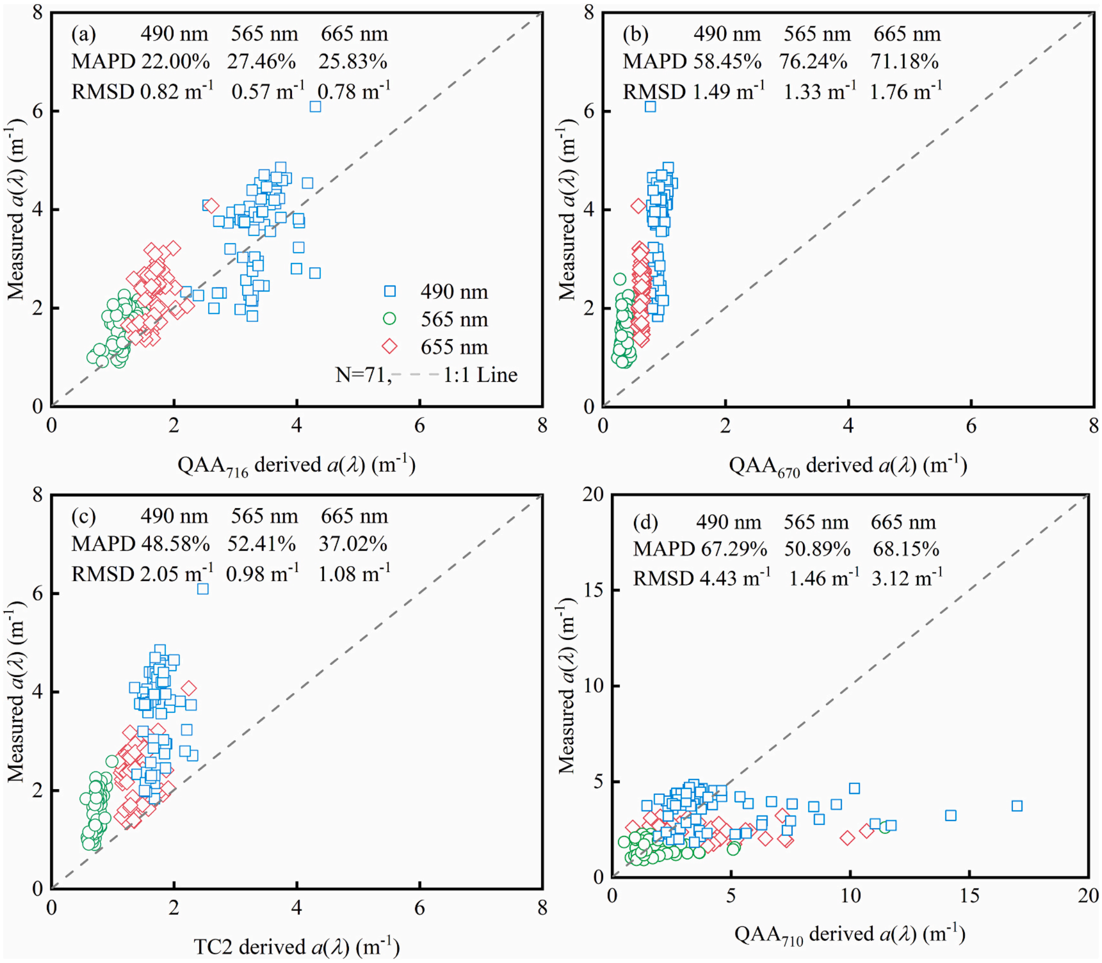

Fig. 2. Validation and comparison of *a* at 490 nm, 565 nm, and 665 nm. (a) The new re-parametrized QAA (QAA_{716}) proposed in this study. (b) The original QAA (QAA_{670}) proposed by Lee et al. (2014a); (c) the improved QAA (TC2) proposed by Liu et al. (2020); (d) QAA_{710} proposed by Huang et al. (2014).

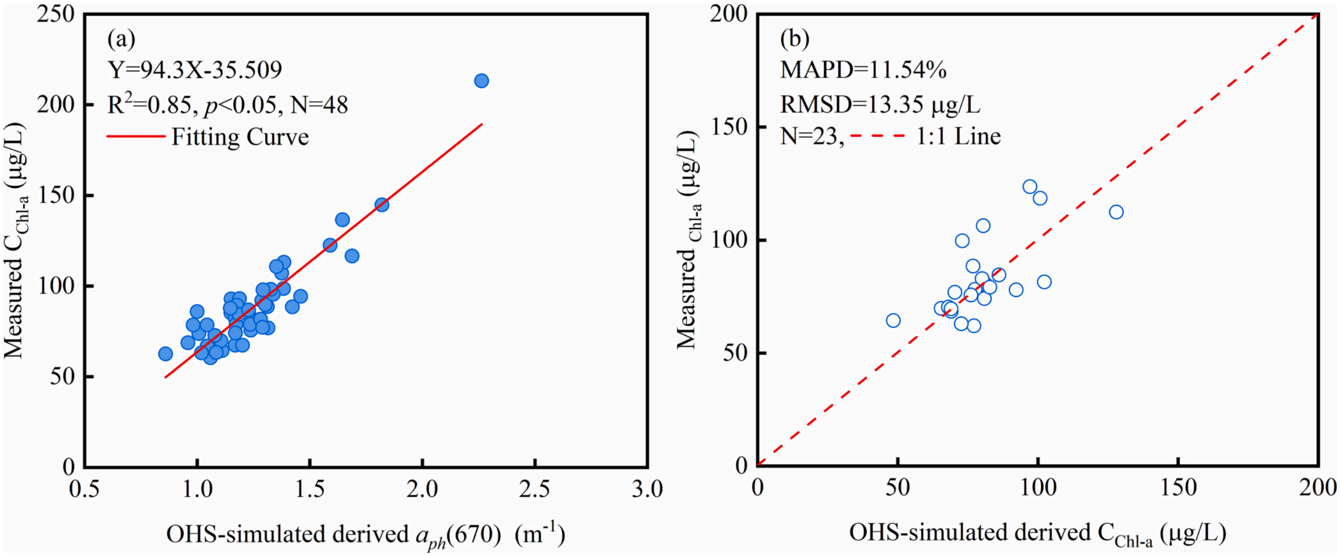

Fig. 3. Calibration and validation of $C_{Chl\text{-}a}$ with $a_{ph}(670)$ based on simulated OHS. (a) Fitting curves of measured $C_{Chl\text{-}a}$ with $a_{ph}(670)$ based on simulated OHS; (b) comparison of measured $C_{Chl\text{-}a}$ with derived $C_{Chl\text{-}a}$ based on simulated OHS.

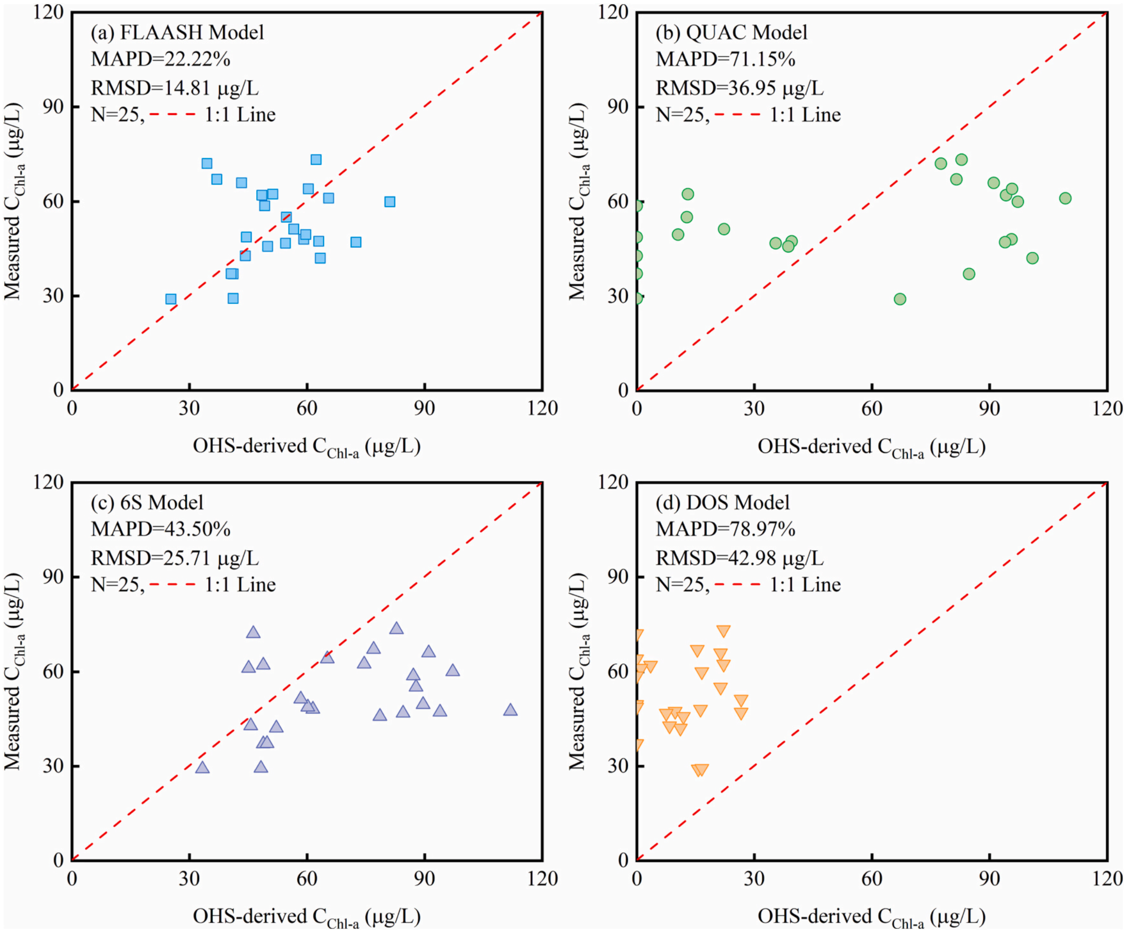

Fig. 4. Validation and comparison of the OHS-derived $C_{Chl\text{-}a}$ with measured $C_{Chl\text{-}a}$ after different atmospheric correction models. (a) FLAASH model; (b) QUAC model; (c) 6S model; (d) DOS model.

Table 2

The measured water quality parameters and optical parameters in Dianchi Lake. S.D. is the standard deviation. C.V. is the coefficient of variation.

Sampling time	Parameters	Max	Min	Mean	S.D.	C.V.	Usage
2017/04 (N = 32)	Chl-a (μg/L)	106.18	61.86	81.52	15.34	18.82 %	Model development and validation[a]
	TSM (mg/L)	53.75	21.33	33.70	6.00	17.80 %	
	SD (m)	0.60	0.20	0.32	0.07	21.88 %	
	TN (mg/L)	2.70	1.66	2.15	0.23	10.70 %	
	TP (mg/L)	0.21	0.09	0.14	0.02	14.29 %	
	$a_{ph}(490)$ (m^{-1})	2.66	1.28	2.16	0.25	11.57 %	
	$a_{NAP}(490)$ (m^{-1})	2.21	0.86	1.65	0.32	19.39 %	
	$a_{CDOM}(490)$ (m^{-1})	0.24	0.11	0.18	0.03	16.67 %	
2017/11 (N = 39)	Chl-a	213.13	60.18	90.35	29.02	32.12 %	
	TSM	59.38	29.50	36.03	6.30	17.49 %	
	SD	0.54	0.24	0.38	0.06	15.79 %	
	TN	4.18	2.00	2.55	0.42	16.47 %	
	TP	0.25	0.04	0.09	0.04	44.44 %	
	$a_{ph}(490)$	4.42	0.93	1.90	0.73	38.42 %	
	$a_{nan}(490)$	1.80	0.61	1.13	0.40	35.40 %	
	$a_{CDOM}(490)$	0.70	0.10	0.31	0.14	45.16 %	
2019/04/02 (N = 9)	Chl-a	72	29	53.56	14.14	26.40 %	Satellite synchronous validation[b]
2021/03/19 (N = 5)		62	29	48	11.31	23.57 %	
2021/03/26 (N = 4)		73	47	61.5	9.55	15.53 %	
2021/04/16 (N = 7)		59	37	47.86	6.01	12.56 %	

[a] Seventy-one optical data were used to improve and validate the QAA (Table 1, Fig. 2). Seventy-one Chl-a data were used to calibrate and validate the Chl-a semi-analytical model (Fig. 3), as well as to compare with existing algorithms (Figs. S5, S6, Table S1). Seventy-one TSM, SD, TN, and TP data were used to analyze the driving forces of $C_{Chl\text{-}a}$ (Fig. S3).

[b] In those data, which came from Dianchi Lake Administration and China National Environmental Monitoring Centre, only $C_{Chl\text{-}a}$ data were measured in synchronization with OHS images, validating the OHS-derived $C_{Chl\text{-}a}$ (Fig. 4).

3. Results

3.1. Water quality parameters and optical properties

Dianchi Lake exhibited high $C_{\text{Chl-a}}$ (>80 μg/L on average) during two field campaigns and a high percentage of a_{ph}. The variability of $C_{\text{Chl-a}}$ in autumn (32.12 %) was higher than that seen in spring (18.82 %). TSM and SD remained at prominent levels with low variability in both seasons. Additionally, Dianchi Lake had an abundance of TN and TP, supporting the rapid growth of algae. The lake's optical properties were more variable and received stronger seasonal influences, especially when obtained in autumn. In conclusion, the elevated content of Chl-a, TSM, a_{ph}, and organic matters, along with the low SD, indicates that Dianchi Lake is an extremely turbid and Chl-a-dominated eutrophic lake.

In this study, a total of twenty-five $C_{\text{Chl-a}}$ measurements were collected synchronously with OHS observations. The measurements covered a wide range of $C_{\text{Chl-a}}$, ranging from the lowest value of 29 μg/L to the highest value of 73 μg/L (Table 2).

3.2. Validation and calibration of the semi-analytical model

3.2.1. Validation of QAA_{716}

To demonstrate the applicability and uncertainty of the QAA_{716}, we compared its performance to those of QAA_{670} and two other modified QAAs proposed by Liu et al. (2020) (TC2) and Huang et al. (2014) (QAA_{710}). Fig. 2 compares seventy-one derived a from QAAs with the measured a at 490 nm, 565 nm, and 655 nm. The QAA_{716} had the best estimation accuracy (MAPD ranged from 22.00 % to 27.46 %, and RMSD ranged from 0.57 m^{-1} to 0.82 m^{-1}). The QAA_{670} estimations were found to be extremely poor and significantly underestimated (MAPD ranged from 58.45 % to 76.24 %, and RMSD ranged from 1.33 m^{-1} to 1.76 m^{-1}). The TC2 estimations for each band were better than the QAA_{670}, but still significantly underestimated (MAPD ranged from 37.02 % to 52.41 %, and RMSD ranged from 0.98 m^{-1} to 2.05 m^{-1}). The QAA_{710} estimations were significantly overestimated, especially for 490 nm, and its bias was higher than that of the QAA_{670} (MAPD ranged from 50.89 % to 68.15 %, and RMSD ranged from 1.46 m^{-1} to 4.43 m^{-1}). The results of QAA_{716} were practically along the 1:1 line, achieving more satisfactory results than the other QAAs, and the deviation from the measured data was within the acceptable band.

3.2.2. Calibration and validation of the OHS-simulated Chl-a estimation model

To construct a Chl-a estimation model, Fig. S2 analyzed the correlation between OHS-simulated derived a_{ph} and $C_{\text{Chl-a}}$. The highest correlation coefficient was found at $B14$ ($r = 0.88$), with the $B14$ central wavelength of the OHS at 670 nm. A relationship was constructed using $a_{ph}(670)$ and $C_{\text{Chl-a}}$. Fig. 3 depicts the calibrated and validated model for estimating $C_{\text{Chl-a}}$, demonstrating the excellent performance of the proposed $C_{\text{Chl-a}}$ estimation model based on simulated OHS image (MAPD = 11.54 %, RMSD = 13.35 μg/L). The data points were roughly located along the 1:1 line, showing that the proposed model in this study could be applied to the retrieval of $C_{\text{Chl-a}}$ data from OHS images. The following $C_{\text{Chl-a}}$ estimation model was constructed based on simulated OHS:

$$C_{Chl-a} = 94.3 \times a_{ph}(670) - 35.509 \tag{16}$$

where $a_{ph}(670)$ is the a_{ph} at 670 nm obtained using QAA_{716} based on simulated OHS.

3.3. Validation of Chl-a for OHS images

Twenty-five uniformly distributed satellite-ground synchronous $C_{\text{Chl-a}}$ data from Dianchi Lake were used to validate the feasibility of OHS images for the Chl-a semi-analytical model. Furthermore, the FLAASH, QUAC, 6S, and DOS models were used to evaluate the impact of different AC models on the Chl-a semi-analytical model. As seen in Fig. 4, the FLAASH model yielded the best results (MAPD = 22.22 %, RMSD = 14.81 μg/L) and could be applied to OHS images. Conversely, the QUAC and the DOS models led to the overestimation and underestimation of $C_{\text{Chl-a}}$, respectively, and were not acceptable. The AC results were consistent with the findings of Zhang et al. (2021) in Dianchi Lake, indicating that the FLAASH model was a suitable atmospheric correction model for the OHS imagery.

3.4. Spatial-temporal patterns of Chl-a concentration

The spatial-temporal patterns of $C_{\text{Chl-a}}$ in Dianchi Lake from 2019 to 2021, derived from OHS images using our proposed QAA_{716} model, are presented in Fig. 5. Overall, $C_{\text{Chl-a}}$ demonstrated significant spatial-temporal variation in Dianchi Lake. Spatially, the central and south-western parts of Dianchi Lake displayed lower $C_{\text{Chl-a}}$ levels, while the northern part of Dianchi Lake exhibited higher $C_{\text{Chl-a}}$ levels. This finding is consistent with the studies conducted by Bi et al. (2019). Briefly, the average $C_{\text{Chl-a}}$ was higher in 2021 (75.14 μg/L) than in 2020 (60.88 μg/L) and 2019 (50.00 μg/L). The highest $C_{\text{Chl-a}}$ (102.62 μg/L) was observed on September 13, 2021, while the lowest $C_{\text{Chl-a}}$ (41.40 μg/L) was observed on November 24, 2020. According to the Kunming Environmental Monitoring Centre, the multi-year average $C_{\text{Chl-a}}$ in Dianchi was reported as 83.67 ± 39.95 μg/L (Mu, 2020).

4. Discussion

4.1. Comparing with existing algorithms

We reselected the reference band to be 716 nm, based on the optical characteristics of Dianchi Lake, and then conducted a re-parameterization. Compared to the QAA_{670}, the QAA_{716} displayed a significant reduction in the MAPD (from 58.45 %–76.24 % to 22.00 %–27.46 %), resulting in a more robust estimation. The QAA_{716} also outperformed the TC2 and QAA_{710}. Fig. 2 illustrates the necessity of reselecting the reference band and conducting re-parameterization when using the QAA model in Dianchi Lake.

Additionally, we compared the Chl-a estimation model using the QAA_{716} alongside the more commonplace Chl-a estimation models, based on in-situ data from Dianchi Lake (Table S1). Table S1 indicates that the semi-analytical model proposed in this study had the highest R^2 and the best estimation accuracy ($R^2 = 0.85$, MAPD = 11.54 %, RMSD = 13.35 μg/L). Overall, it provides a novel approach for Chl-a detection in inland waters. Liu et al. (2020) considered $a^*_{ph}(665)$ to be equal to 0.017 m^2mg^{-1} based on global data collection. However, the accuracy of $a^*_{ph}(665)$ for Chl-a estimation in Dianchi Lake was unsatisfactory compared to the model used in this study. By modifying the parameters based on measured data, it is possible to develop a more applicable model. Further study should be conducted to determine the applicability of the values of a^*_{ph} using the extensive data collected from Dianchi Lake. Such research could assess the applicability and generality of the Chl-a model and QAA_{716} to other types of inland waters.

4.2. Driving forces

4.2.1. Relationship between Chl-a concentration and water quality parameters

Fig. S3 shows the relationship between $C_{\text{Chl-a}}$ and water quality parameters. $C_{\text{Chl-a}}$ showed a weak correlation with transparency ($r = 0.20$, $p > 0.05$) and a significant positive correlation with TSM ($r = 0.60$, $p < 0.05$), both of which were associated with the underwater light environment. This indicates that the increased $C_{\text{Chl-a}}$ was related to the degradation of the underwater light environment in Dianchi Lake, which is consistent with Zhang et al.'s (2016) study. TN and TP are important

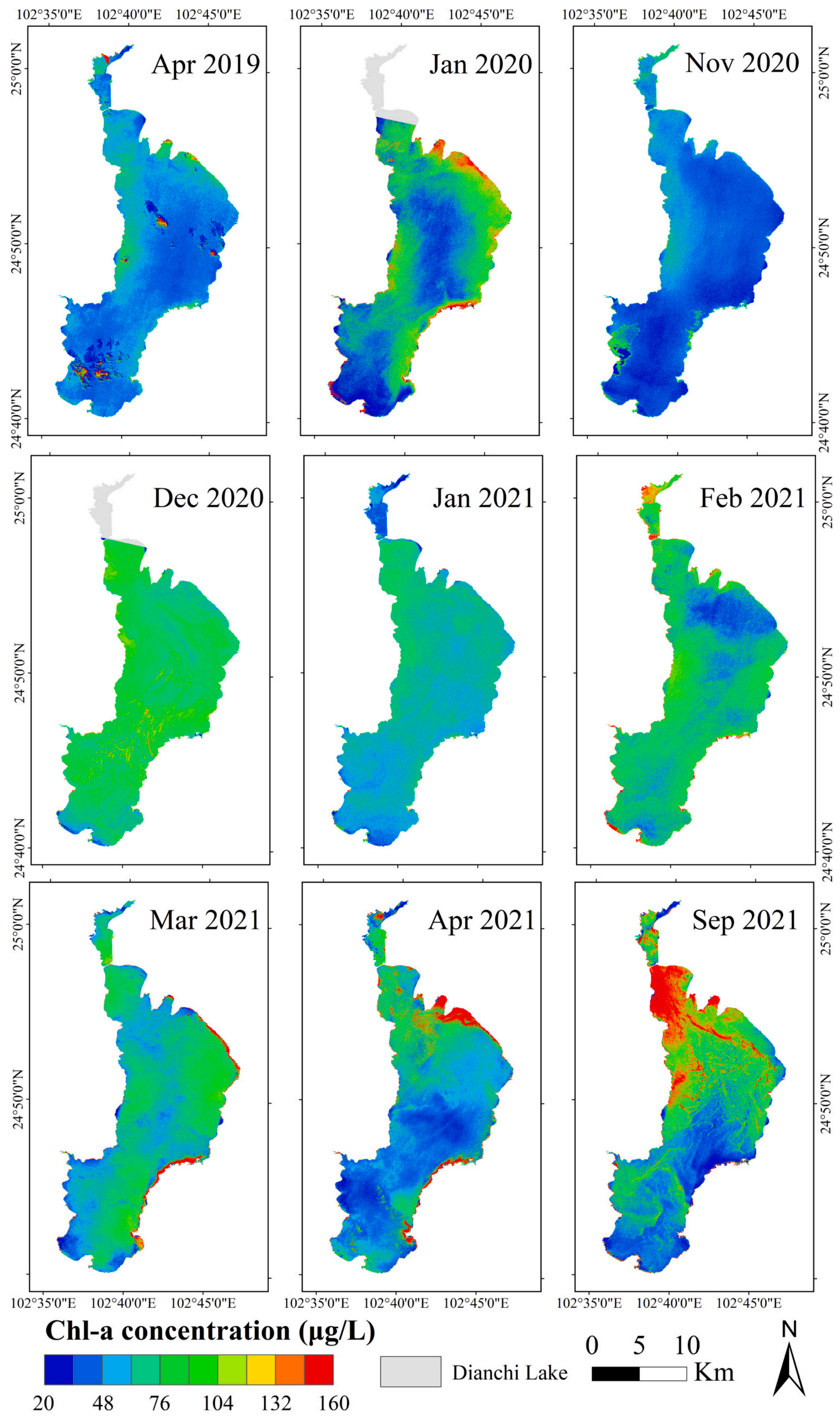

Fig. 5. The spatial-temporal patterns of OHS-derived $C_{\text{Chl-a}}$ in Dianchi Lake from 2019 to 2021.

nutrients for phytoplankton growth (Yang et al., 2016). In the case of Dianchi Lake, it receives nutrients from its surroundings, resulting in the TN and TP concentrations that are sufficient to support normal algal growth. This, in turn, affects the variations in $C_{\text{Chl-a}}$. The correlation between $C_{\text{Chl-a}}$ and TN ($r = 0.77$, $p < 0.05$) was stronger than the correlation between $C_{\text{Chl-a}}$ and TP ($r = 0.36$, $p > 0.05$), which could be attributed to the dominant algal species present in Dianchi Lake.

4.2.2. *Relationship between Chl-a concentration and climatic factors*

Fig. S4 analyzes the relationship between OHS-derived $C_{\text{Chl-a}}$ in Dianchi Lake and climatic factors during the month of study. The relationship between $C_{\text{Chl-a}}$, temperatures ($r = 0.32$, $p > 0.05$), and wind ($r = 0.26$, $p > 0.05$) were found to be insignificant, which could be attributed to the short-term nature of the observations. However, there was a significant correlation ($r = 0.60$, $p < 0.05$) between $C_{\text{Chl-a}}$ and precipitation. Previous studies (Reichwaldt and Ghadouani, 2012) have confirmed that rainfall can result in a transient increase in nutrients, promoting the increase in $C_{\text{Chl-a}}$. This phenomenon was observed in Dianchi Lake (Mu et al., 2019).

In summary, the strongest correlations with TN and the transient increase in nutrients caused by precipitation are both related to the promotion of nutrient inputs. This indicates that the $C_{\text{Chl-a}}$ in Dianchi Lake is primarily influenced by the input of nutrients. Controlling nutrient input could effectively reduce $C_{\text{Chl-a}}$.

4.3. *Radiometric performance of OHS image*

Fig. 6 compares the SNR and $NE_{Chl\text{-}a}$ for various images, most of which were designed for marine and continental applications. In Fig. 6a, the SNR of MODIS (Moderate-resolution Imaging Spectroradiometer) (Barnes et al., 2003), MERIS (Medium Resolution Imaging Spectrometer) (Morel, 1998), OLCI (Ocean and Land Colour Instrument) (Shimoda et al., 2012), and OLI2 were significantly higher than those of OHS and Hyperion. This was due to wider bandwidth, coarser spatial resolution, and higher radiation energy intake. Compared to Hyperion, another hyperspectral satellite, OHS had a higher spatial resolution and overall higher SNR. However, the low SNR of OHS at 760 nm may result in significant deviations when the QAA_{716} was applied. Fig. 6b showed that Hyperion (81.28 μg/L on average) and OHS (72.86 μg/L on average) had comparable $NE_{Chl\text{-}a}$, while OLCI (55.44 μg/L on average), MODIS (35.72 μg/L on average), and MERIS (40.49 μg/L) had relatively lower $NE_{Chl\text{-}a}$. A high SNR in each spectral band is crucial for accurately estimating water quality parameters. Compared to Hyperion, OHS had a higher overall SNR, which resulted in lower $NE_{Chl\text{-}a}$. On the other hand, OLCI, which is the successor of MERIS, exhibited a relatively high SNR. In spite of that, OLCI had a high overall $NE_{Chl\text{-}a}$ due to the low SNR at 760 nm.

According to previous studies (Hu et al., 2012a; Lee et al., 2014b), a high SNR in a satellite sensor can be achieved by having a low spatial resolution (e.g., 1000 m for MODIS) or a wide spectral band (e.g., 50–100 nm for Landsat). This allows enough photons to ensure image quality. OHS, with its high spatial and high spectral resolution, radiated less energy, possessed stable state photons, and had a low, predictable SNR. However, it still had better overall SNR compared to Hyperion. $NE_{Chl\text{-}a}$ is a quantity that varies with the solar zenith angle (θ, Eq. (12)). However, when the semi-analytical model proposed in this study was used, the relationship between $NE_{Chl\text{-}a}$ and θ was not evident (Fig. 6b). This finding contradicts the results of Vanhellemont and Ruddick (2014) on noise-equivalent suspended matter in the English Channel. This discrepancy may be caused by the fact that most QAA equations were based on ratio calculations, which indirectly reduced the impact of variations in θ variations on estimates.

In conclusion, the OHS imagery had relatively moderate SNR and $NE_{Chl\text{-}a}$, possibly producing some differences in image applications. However, OHS had significant advantages for remotely estimating $C_{\text{Chl-a}}$ in eutrophic lakes, due to its three high features and overall suitable performance.

5. Conclusions

Based on our study of Dianchi Lake, we completed the rate determination and re-parameterization of the reference band in QAA. Then, we evaluated the feasibility and applicability of OHS for estimating $C_{\text{Chl-a}}$. QAA_{716} demonstrated significantly higher accuracy compared to QAA_{670}, TC2, and QAA_{710}, with MAPD reduced to 22.00 %–27.46 % and RMSD reduced to 0.57 m^{-1}–0.82 m^{-1}. Among the tested Chl-a estimation models for $C_{\text{Chl-a}}$, the one with $a_{ph}(670)$ as a proxy parameter performed the best, with MAPD of 11.54 % and RMSD of 13.35 μg/L. When applied to OHS images, the FLAASH model was preferred over the QUAC, 6S, and DOS models, with MAPD of 22.22 % and RMSD of 14.81 μg/L. The improved SNR of OHS image promoted the capability of Chl-a estimation. The increased $C_{\text{Chl-a}}$ in Dianchi Lake was primarily associated with the nutrients input, showing a significant positive correlation with total nitrogen. In summary, the semi-analytical model proposed in this study can be applied to estimate $C_{\text{Chl-a}}$ in inland eutrophic waters. OHS, as an orbiting hyperspectral satellite with three high features, could effectively capture the spectral features and spatial details in water bodies, providing a new tool for monitoring inland waters.

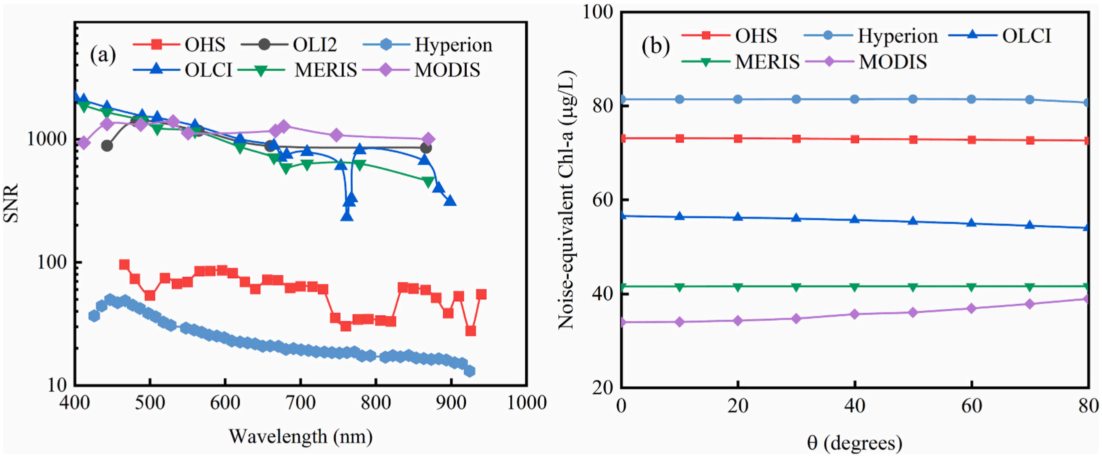

Fig. 6. Comparison of SNR and $NE_{Chl\text{-}a}$ of OHS images with that of other mainstream images. (a) SNR comparison of various images; (b) variation of $NE_{Chl\text{-}a}$ with solar zenith angle for various images.

CRediT authorship contribution statement

Zhubin Zheng: Conceptualization, Writing - original draft, review & editing, Methodology, Investigation, Funding acquisition, Supervision.
Chao Huang: Writing - original draft, review & editing, Software, Methodology, Visualization, Validation.
Yunmei Li: Writing - review & editing, Methodology, Funding acquisition, Supervision.
Heng Lyu: Writing - review, Methodology, Validation.
Changchun Huang: Writing - review, Methodology, Validation.
Na Chen: Writing - review & editing, Resources.
Ge Liu: Resources, Investigation, Funding acquisition.
Yulong Gu: Writing - review & editing, Resources.
Shaohua Lei: Methodology, Investigation, Funding acquisition.
Runfei Zhang: Software, Writing - review & editing, Visualization.
Jianzhong Li: Software, Writing - review & editing, Validation.

Declaration of competing interest

The authors declare that they have no known competing financial interests or personal relationships that could have appeared to influence the work reported in this paper.

Data availability

Data will be made available on request.

Acknowledgements

This research was funded by the National Natural Science Foundation of China-Yunnan Joint Fund (U2102207), the National Natural Science Foundation of China (No. 41701412; 42071299; 42171385 and 42101384), the Social Science Foundation of Jiangxi Province (No. 22GL27), the Humanities and Social Sciences Project of Jiangxi Provincial University (No. GL21143), the Science and Technology Project of Jiangxi Provincial Education Department (No. GJJ2201216). The field measurement data of this study were obtained from the Water Environment Remote Sensing Research Group of the Key Laboratory of Virtual Geographical Environment the Ministry of Education of Nanjing Normal University. We sincerely thank the hard work of the experiment-related personnel of Nanjing Normal University. We greatly thank for the hyperspectral images data support from Zhuhai Orbita Aerospace Technology Co., Ltd., and the Dianchi Lake Administration and China National Environmental Monitoring Centre for providing the in-situ Chlorophyll-a concentration data, respectively. We are deeply grateful to the associate editor Professor Ashantha Goonetilleke and the three anonymous reviewers for their constructive comments and suggestions to improve the quality of this work.

Appendix A. Supplementary data

Supplementary data to this article can be found online at https://doi.org/10.1016/j.scitotenv.2023.166785.

References

Barnes, W.L., Xiong, X., Salomonson, V.V., 2003. Status of terra MODIS and aqua modis. Adv. Space Res. 32, 2099–2106. https://doi.org/10.1016/S0273-1177(03)90529-1.

Beck, R., Zhan, S.G., Liu, H.X., Tong, S., Yang, B., Xu, M., et al., 2016. Comparison of satellite reflectance algorithms for estimating chlorophyll-a in a temperate reservoir using coincident hyperspectral aircraft imagery and dense coincident surface observations. Remote Sens. Environ. 178, 15–30. https://doi.org/10.1016/j.rse.2016.03.002.

Bi, S., Li, Y., Lv, H., Zhu, L., Mu, M., Lei, S., et al., 2018a. Estimation of chlorophyll-a concentration in Lake Erhai based on OLCI data. J. Lake Sci. 30, 701–712. https://doi.org/10.18307/2018.0312 (in Chinese).

Bi, S., Li, Y., Wang, Q., Lyu, H., Liu, G., Zheng, Z., et al., 2018b. Inland water atmospheric correction based on turbidity classification using OLCI and SLSTR synergistic observations. Remote Sens. 10. https://doi.org/10.3390/rs10071002.

Bi, S., Li, Y., Lyu, H., Mu, M., Xu, J., Lei, S., et al., 2019. Quantifying spatiotemporal dynamics of the column-integrated algal biomass in nonbloom conditions based on OLCI data: a case study of Lake Dianchi, China. IEEE Trans. Geosci. Remote Sens. 57, 7447–7459. https://doi.org/10.1109/TGRS.2019.2913401.

Bresciani, M., Giardino, C., Fabbretto, A., Pellegrino, A., Mangano, S., Free, G., et al., 2022. Application of new hyperspectral sensors in the remote sensing of aquatic ecosystem health: exploiting PRISMA and DESIS for four Italian lakes. Resources 11. https://doi.org/10.3390/resources11020008.

Brian Gregory, M., 1990. Algorithms for determining the absorption coefficient for aquatic particulates using the quantitative filter technique. Proc.SPIE 1302, 137–148. https://doi.org/10.1117/12.21440.

Bricaud, A., Babin, M., Morel, A., Claustre, H., 1995. Variability in the chlorophyll-specific absorption coefficients of natural phytoplankton: analysis and parametrization. J. Geophys. Res. 100, 13,321–313,332. https://doi.org/10.1029/95JC00463.

Cao, Z., Duan, H., Song, Q., Shen, M., Ma, R., Liu, D., 2018. Evaluation of the sensitivity of China's next-generation ocean satellite sensor MWI onboard the Tiangong-2 space lab over inland waters. Int. J. Appl. Earth Obs. Geoinf. 71, 109–120. https://doi.org/10.1016/j.jag.2018.05.012.

Cao, Z.G., Ma, R.H., Duan, H.T., Xue, K., 2019. Effects of broad bandwidth on the remote sensing of inland waters: implications for high spatial resolution satellite data applications. ISPRS J. Photogramm. Remote Sens. 153, 110–122. https://doi.org/10.1016/j.isprsjprs.2019.05.001.

Cao, Z., Ma, R., Duan, H., Pahlevan, N., Melack, J., Shen, M., et al., 2020. A machine learning approach to estimate chlorophyll-a from Landsat-8 measurements in inland lakes. Remote Sens. Environ. 248. https://doi.org/10.1016/j.rse.2020.111974.

Cao, Z., Ma, R., Pahlevan, N., Liu, M., Melack, J., Duan, H., et al., 2022a. Evaluating and optimizing VIIRS retrievals of chlorophyll-a and suspended particulate matter in turbid lakes using a machine learning approach. IEEE Trans. Geosci. Remote Sens. 60, 1–17. https://doi.org/10.1109/TGRS.2022.3220529.

Cao, Z.G., Ma, R.H., Liu, M., Duan, H.T., Xiao, Q., Xue, K., et al., 2022b. Harmonized chlorophyll-a retrievals in inland lakes from Landsat-8/9 and sentinel 2A/B virtual constellation through machine learning. IEEE Trans. Geosci. Remote Sens. 60, 1–16. https://doi.org/10.1109/Tgrs.2022.3207345.

Ciotti, Á.M., Lewis, M.R., Cullen, J.J., 2002. Assessment of the relationships between dominant cell size in natural phytoplankton communities and the spectral shape of the absorption coefficient. Limnol. Oceanogr. 47, 404–417. https://doi.org/10.4319/lo.2002.47.2.0404.

Cleveland, J.S., 1995. Regional models for phytoplankton absorption as a function of chlorophyll a concentration. J. Geophys. Res. Oceans 100, 13333–13344. https://doi.org/10.1029/95JC00532.

Ekstrand, S., 1992. Landsat TM based quantification of chlorophyll-a during algae blooms in coastal waters. Int. J. Remote Sens. 13, 1913–1926. https://doi.org/10.1080/01431169208904240.

Etheridge, J.R., Birgand, F., Osborne, J.A., Osburn, C.L., Burchell Ii, M.R., Irving, J., 2014. Using in situ ultraviolet-visual spectroscopy to measure nitrogen, carbon, phosphorus, and suspended solids concentrations at a high frequency in a brackish tidal marsh. Limnol. Oceanogr. Methods 12, 10–22. https://doi.org/10.4319/lom.2014.12.10.

Hu, C., Feng, L., Lee, Z., Davis, C.O., Mannino, A., McClain, C.R., et al., 2012a. Dynamic range and sensitivity requirements of satellite ocean color sensors: learning from the past. Appl. Opt. 51, 6045–6062. https://doi.org/10.1364/AO.51.006045.

Hu, C.M., Lee, Z., Franz, B., 2012b. Chlorophyll a algorithms for oligotrophic oceans: a novel approach based on three-band reflectance difference. J. Geophys. Res. Oceans 117, C01011. https://doi.org/10.1029/2011JC007395.

Huang, J., Chen, L., Chen, X., Tian, L., Feng, L., Yesou, H., et al., 2014. Modification and validation of a quasi-analytical algorithm for inherent optical properties in the turbid waters of Poyang Lake, China. J. Appl. Remote. Sens. 8, 083643 https://doi.org/10.1117/1.JRS.8.083643.

Huang, C., Guo, Y., Yang, H., Li, Y., Zou, J., Zhang, M., et al., 2015. Using remote sensing to track variation in phosphorus and its interaction with chlorophyll-a and suspended sediment. IEEE J. Sel. Top. Appl. Earth Observ. Remote Sensing 8, 4171–4180. https://doi.org/10.1109/JSTARS.2015.2438293.

Jespersen, A.-M., Christoffersen, K., 1987. Measurements of chlorophyll-a from phytoplankton using ethanol as extraction solvent. Arch. Hydrobiol. 109, 445–454. https://doi.org/10.1127/archiv-hydrobiol/109/1987/445.

Jiang, D., Matsushita, B., Pahlevan, N., Gurlin, D., Lehmann, M.K., Fichot, C.G., et al., 2021. Remotely estimating total suspended solids concentration in clear to extremely turbid waters using a novel semi-analytical method. Remote Sens. Environ. 258, 112386 https://doi.org/10.1016/j.rse.2021.112386.

Kutser, T., Herlevi, A., Kallio, K., Arst, H., 2001. A hyperspectral model for interpretation of passive optical remote sensing data from turbid lakes. Sci. Total Environ. 268, 47–58. https://doi.org/10.1016/S0048-9697(00)00682-3.

Le, C., Li, Y., Zha, Y., Sun, D., Yin, B., 2009. Validation of a quasi-analytical algorithm for highly turbid eutrophic water of Meiliang Bay in Taihu Lake, China. IEEE Trans. Geosci. Remote Sens. 47, 2492–2500. https://doi.org/10.1109/tgrs.2009.2015658.

Le, C., Hu, C., Cannizzaro, J., English, D., Muller-Karger, F., Lee, Z., 2013. Evaluation of chlorophyll-a remote sensing algorithms for an optically complex estuary. Remote Sens. Environ. 129, 75–89. https://doi.org/10.1016/j.rse.2012.11.001.

Lee, Z., Carder, K.L., Steward, R., Peacock, T., Davis, C., Patch, J., 1998. An empirical algorithm for light absorption by ocean water based on color. J. Geophys. Res. Oceans 103, 27967–27978. https://doi.org/10.1029/98JC01946.

Lee, Z., Carder, K.L., Arnone, R.A., 2002. Deriving inherent optical properties from water color: a multiband quasi-analytical algorithm for optically deep waters. Appl. Opt. 41, 5755–5772. https://doi.org/10.1364/AO.41.005755.

Lee, Z., Lubac, B., Werdell, J., Arnone, R., 2014a. Update of the quasi-analytical algorithm (QAA_v6)[R/OL]. 2023. https://ioccg.org/groups/software.html.

Lee, Z., Shang, S., Hu, C., Zibordi, G., 2014b. Spectral interdependence of remote-sensing reflectance and its implications on the design of ocean color satellite sensors. Appl. Opt. 53, 3301–3310. https://doi.org/10.1364/AO.53.003301.

Lee, Z., Shang, S., Qi, L., Yan, J., Lin, G., 2016. A semi-analytical scheme to estimate Secchi-disk depth from Landsat-8 measurements. Remote Sens. Environ. 177, 101–106. https://doi.org/10.1016/j.rse.2016.02.033.

Li, J., Gao, M., Feng, L., Zhao, H., Shen, Q., Zhang, F., et al., 2019. Estimation of chlorophyll-a concentrations in a highly turbid eutrophic lake using a classification-based MODIS land-band algorithm. IEEE J. Sel. Top. Appl. Earth Observ. Remote Sensing 12, 3769–3783. https://doi.org/10.1109/JSTARS.2019.2936403.

Li, J., Zheng, Z., Liu, G., Chen, N., Lei, S., Du, C., et al., 2023. Estimating effects of natural and anthropogenic activities on trophic level of inland water: analysis of Poyang Lake Basin, China, with Landsat-8 observations. Remote Sens. 15. https://doi.org/10.3390/rs15061618.

Lima, T.M., Giardino, C., Bresciani, M., Barbosa, C.C., Fabbretto, A., Pellegrino, A., et al., 2023. Assessment of estimated phycocyanin and chlorophyll-a concentration from PRISMA and OLCI in Brazilian inland waters: a comparison between semi-analytical and machine learning algorithms. Remote Sens. 15. https://doi.org/10.3390/rs15051299.

Liu, F., Tang, S., 2019. Evaluation of red-peak algorithms for chlorophyll measurement in the Pearl River Estuary. IEEE Trans. Geosci. Remote Sens. 57, 8928–8936. https://doi.org/10.1109/TGRS.2019.2923754.

Liu, W., Wang, S., Zhang, L., Ni, Z., 2015. Water pollution characteristics of Dianchi Lake and the course of protection and pollution management. Environ. Earth Sci. 74, 3767–3780. https://doi.org/10.1007/s12665-015-4152-x.

Liu, G., Li, L., Song, K., Li, Y., Lyu, H., Wen, Z., et al., 2020. An OLCI-based algorithm for semi-empirically partitioning absorption coefficient and estimating chlorophyll a concentration in various turbid case-2 waters. Remote Sens. Environ. 239, 111648 https://doi.org/10.1016/j.rse.2020.111648.

Lyu, H., Li, X., Wang, Y., Jin, Q., Cao, K., Wang, Q., et al., 2015. Evaluation of chlorophyll-a retrieval algorithms based on MERIS bands for optically varying eutrophic inland lakes. Sci. Total Environ. 530-531, 373–382. https://doi.org/10.1016/j.scitotenv.2015.05.115.

Mishra, S., Mishra, D.R., Lee, Z., Tucker, C.S., 2013. Quantifying cyanobacterial phycocyanin concentration in turbid productive waters: a quasi-analytical approach. Remote Sens. Environ. 133, 141–151. https://doi.org/10.1016/j.rse.2013.02.004.

Mobley, C.D., 1999. Estimation of the remote-sensing reflectance from above-surface measurements. Appl. Opt. 38, 7442–7455. https://doi.org/10.1364/AO.38.007442.

Morel, A., 1998. Minimum Requirements for an Operational, Ocean-Colour Sensor for the Open Ocean.

Mu, M., 2020. Study of Algal Bloom Occurrence Probability Prediction Model Based on Remote Sensing Data and Meteorological Factors in Dianchi Lake. Nanjing Normal University (in Chinese, PHD thesis).

Mu, M., Wu, C., Li, Y., Lyu, H., Fang, S., Yan, X., et al., 2019. Long-term observation of cyanobacteria blooms using multi-source satellite images: a case study on a cloudy and rainy lake. Environ. Sci. Pollut. Res. 26, 11012–11028. https://doi.org/10.1007/s11356-019-04522-6.

Mueller, J., Morel, A., Frouin, R., Davis, C., Arnone, R., Carder, K., et al., 2003. Ocean Optics Protocols for Satellite Ocean Color Sensor Validation, Revision 4, Volume III: Radiometric Measurements and Data Analysis Protocols.

Nardelli, S., Twardowski, M., 2016. Assessing the link between chlorophyll concentration and absorption line height at 676 nm over a broad range of water types. Opt. Express 24, A1374–A1389. https://doi.org/10.1364/OE.24.0A1374.

Ogashawara, I., Mishra, D.R., Nascimento, R.F.F., Alcantara, E.H., Kampel, M., Stech, J. L., 2016. Re-parameterization of a quasi-analytical algorithm for colored dissolved organic matter dominant inland waters. Int. J. Appl. Earth Obs. Geoinf. 53, 128–145. https://doi.org/10.1016/j.jag.2016.09.001.

O'Reilly, J., Maritorena, S., Mitchell, B.G., Siegel, D., Carder, K., Garver, S.A., et al., 1998. Ocean color chlorophyll algorithms for SeaWiFS. J. Geophys. Res. 103, 937–953. https://doi.org/10.1029/98JC02160.

O'Shea, R.E., Pahlevan, N., Smith, B., Bresciani, M., Egerton, T., Giardino, C., et al., 2021. Advancing cyanobacteria biomass estimation from hyperspectral observations: demonstrations with HICO and PRISMA imagery. Remote Sens. Environ. 266, 112693 https://doi.org/10.1016/j.rse.2021.112693.

Preisendorfer, R.W., 1986. Secchi disk science: visual optics of natural waters1. Limnol. Oceanogr. 31, 909–926. https://doi.org/10.4319/lo.1986.31.5.0909.

Prieur, L., Sathyendranath, S., 1981. An optical classification of coastal and oceanic waters based on the specific spectral absorption curves of phytoplankton pigments, dissolved organic matter, and other particulate materials. Limnol. Oceanogr. 26, 671–689. https://doi.org/10.4319/lo.1981.26.4.0671.

Reichwaldt, E.S., Ghadouani, A., 2012. Effects of rainfall patterns on toxic cyanobacterial blooms in a changing climate: between simplistic scenarios and complex dynamics. Water Res. 46, 1372–1393. https://doi.org/10.1016/j.watres.2011.11.052.

Ren, J., Zheng, Z., Li, Y., Lv, G., Wang, Q., Lyu, H., et al., 2018. Remote observation of water clarity patterns in Three Gorges Reservoir and Dongting Lake of China and their probable linkage to the Three Gorges Dam based on Landsat 8 imagery. Sci. Total Environ. 625, 1554–1566. https://doi.org/10.1016/j.scitotenv.2018.01.036.

Rodrigues, T., Alcântara, E., Watanabe, F., Imai, N., 2017. Retrieval of Secchi disk depth from a reservoir using a semi-analytical scheme. Remote Sens. Environ. 198, 213–228. https://doi.org/10.1016/j.rse.2017.06.018.

Shi, K., Zhang, Y., Song, K., Liu, M., Zhou, Y., Zhang, Y., et al., 2019. A semi-analytical approach for remote sensing of trophic state in inland waters: bio-optical mechanism and application. Remote Sens. Environ. 232. https://doi.org/10.1016/j.rse.2019.111349.

Shimoda, H., Nieke, J., Borde, F., Mavrocordatos, C., Berruti, B., Delclaud, Y., et al., 2012. The Ocean and Land Colour Imager (OLCI) for the Sentinel 3 GMES Mission: status and first test results. In: Earth Observing Missions and Sensors: Development, Implementation, and Characterization II.

Tang, J.W., Tian, G.L., Wang, X.Y., Wang, X.M., Song, Q.J., 2004. The methods of water spectra measurement and analysis I: above-water method (in Chinese). J. Remote Sensing 8, 37–44. https://doi.org/10.11834/jrs.20040106.

Vanhellemont, Q., Ruddick, K., 2014. Turbid wakes associated with offshore wind turbines observed with Landsat 8. Remote Sens. Environ. 145, 105–115. https://doi.org/10.1016/j.rse.2014.01.009.

Wang, M., Son, S., Harding, L., 2009. Retrieval of diffuse attenuation coefficient in the Chesapeake Bay and turbid ocean regions for satellite ocean color applications. J. Geophys. Res. Oceans 114. https://doi.org/10.1029/2009JC005286.

Watanabe, F., Mishra, D.R., Astuti, I., Rodrigues, T., Alcantara, E., Imai, N.N., et al., 2016. Parametrization and calibration of a quasi-analytical algorithm for tropical eutrophic waters. ISPRS J. Photogramm. Remote Sens. 121, 28–47. https://doi.org/10.1016/j.isprsjprs.2016.08.009.

Wei, J., Lee, Z., Shang, S., 2016. A system to measure the data quality of spectral remote sensing reflectance of aquatic environments. J. Geophys. Res. Oceans 121, 8189–8207. https://doi.org/10.1002/2016JC012126.

Wei, J., Lee, Z., Shang, S., Yu, X., 2019. Semianalytical derivation of phytoplankton, CDOM, and detritus absorption coefficients from the Landsat 8/OLI reflectance in coastal waters. J. Geophys. Res. Oceans 124, 3682–3699. https://doi.org/10.1029/2019jc015125.

Yang, W., Matsushita, B., Chen, J., Fukushima, T., Ma, R., 2010. An enhanced three-band index for estimating chlorophyll-a in turbid case-II waters: case studies of Lake Kasumigaura, Japan, and Lake Dianchi, China. IEEE Geosci. Remote Sens. Lett. 7, 655–659. https://doi.org/10.1109/LGRS.2010.2044364.

Yang, W., Matsushita, B., Chen, J., Yoshimura, K., Fukushima, T., 2013. Retrieval of inherent optical properties for turbid inland waters from remote-sensing reflectance. IEEE Trans. Geosci. Remote Sens. 51, 3761–3773. https://doi.org/10.1109/TGRS.2012.2220147.

Yang, Z., Zhang, M., Shi, X., Kong, F., Ma, R., Yu, Y., 2016. Nutrient reduction magnifies the impact of extreme weather on cyanobacterial bloom formation in large shallow Lake Taihu (China). Water Res. 103, 302–310. https://doi.org/10.1016/j.watres.2016.07.047.

Yang, K., Yu, Z., Luo, Y., Yang, Y., Zhao, L., Zhou, X., 2018. Spatial and temporal variations in the relationship between lake water surface temperatures and water quality - a case study of Dianchi Lake. Sci. Total Environ. 624, 859–871. https://doi.org/10.1016/j.scitotenv.2017.12.119.

Yao, L., Xiao, C., Li, J., Zhang, F., Wang, S., 2020. Secchi disk depth estimation from China's new generation of GF-5 hyperspectral observations using a semi-analytical scheme. Remote Sens. 12, 1849. https://doi.org/10.3390/rs12111849.

Yin, Z., Li, J., Liu, Y., Xie, Y., Zhang, F., Wang, S., et al., 2021. Water clarity changes in Lake Taihu over 36 years based on Landsat TM and OLI observations. Int. J. Appl. Earth Obs. Geoinf. 102, 102457 https://doi.org/10.1016/j.jag.2021.102457.

Zhang, Y., Liu, X., Yin, Y., Wang, M., Qin BJOe., 2012. A simple optical model to estimate diffuse attenuation coefficient of photosynthetically active radiation in an extremely turbid lake from surface reflectance. Opt. Express 20, 20482–20493. https://doi.org/10.1364/OE.20.020482.

Zhang, Y., Liu, X., Qin, B., Shi, K., Deng, J., Zhou, Y., 2016. Aquatic vegetation in response to increased eutrophication and degraded light climate in Eastern Lake Taihu: implications for lake ecological restoration. Sci. Rep. 6, 23867. https://doi.org/10.1038/srep23867.

Zhang, R., Zheng, Z., Liu, G., Du, C., Du, C., Lei, S., et al., 2021. Simulation and assessment of the capabilities of Orbita Hyperspectral (OHS) imagery for remotely monitoring chlorophyll-a in eutrophic plateau lakes. Remote Sens. 13. https://doi.org/10.3390/rs13142821.

Zheng, Z., 2018. Analysis of Spatial and Temporal Patterns of Underwater Light Field and Its Driving Forces in Dongting Lake, China: An Optics and Remote Sensing Approach. Nanjing Normal Univeristy (in Chinese, PHD thesis).

Zheng, Z., Ren, J., Li, Y., Huang, C., Liu, G., Du, C., et al., 2016. Remote sensing of diffuse attenuation coefficient patterns from Landsat 8 OLI imagery of turbid inland waters: a case study of Dongting Lake. Sci. Total Environ. 573, 39–54. https://doi.org/10.1016/j.scitotenv.2016.08.019.

Zheng, Z.B., Zhang, R.F., Li, J.Z., Lin, L., Yang, H., 2022. Remote sensing retrieval of chlorophyll-a concentration in Dianchi lake based on orbita hyperspectral imagery. Natl. Remote Sensing Bull. 26 https://doi.org/10.11834/jrs.20211264 (in Chinese).

Zhong, Y., Wang, X., Wang, S., Zhang, L., 2021. Advances in spaceborne hyperspectral remote sensing in China. Geo-spatial Inf. Sci. 24, 95–120. https://doi.org/10.1080/10095020.2020.1860653.